B21115

Andreas Leineweber*, Marius Holger Wetzel, Stefan Martin, Shun-Li Shang, Zi-Kui Liu

Preparation of $CoGe_2$-type $NiSn_2$ at 10 GPa

https://doi.org/10.1515/znb-2021-0115

Received August 14, 2021; accepted August 23, 2021

***Corresponding author: Andreas Leineweber,** Institute of Materials Science, TU Bergakademie Freiberg, Gustav Zeuner Straße 5, 09599 Freiberg, Germany, and Freiberg High-Pressure Research Centre, Lessingstraße 45, 09599 Freiberg, Germany, e-mail: andreas.leineweber@iww.tu-freiberg.de

Marius Wetzel: Institute of Materials Science, TU Bergakademie Freiberg, Gustav Zeuner Straße 5, 09599 Freiberg, Germany, and Freiberg High-Pressure Research Centre, Lessingstraße 45, 09599 Freiberg, Germany

Stefan Martin: Institute of Materials Science, TU Bergakademie Freiberg, Gustav Zeuner Straße 5, 09599 Freiberg, Germany

Shun-Li Shang and Zi-Kui Liu: Department of Materials Science and Engineering, The Pennsylvania State University, University Park, PA 16802, USA

Professor Richard Dronskowski zum 60. Geburtstag gewidmet

Abstract: An unprecedented $NiSn_2$ intermetallic with $CoGe_2$-type crystal structure has been recovered (at ambient conditions) after high-pressure high-temperature treatment of a $Ni_{33}Sn_{67}$ precursor alloy at 10 GPa and 400°C. The orthorhombic structure with *Aeam* space group symmetry is pseudotetragonal. Based on the evaluation of powder X-ray diffraction data, lattice parameters of $a = b = 6.2818$ Å and $c = 11.8960$ Å have been determined. Complicated line broadening and results of a further microstructure analysis, however, imply a defective character of the crystal structure. First-principles calculations with different model structures and a comparison with structural trends in the literature suggest that at the high-pressure high-temperature conditions a $CuAl_2$-type crystal structure might be stable, which transforms to the recovered $CoGe_2$-type crystal structure upon cooling or the release of pressure.

Keywords: Intermetallic compounds; Soldering; High-pressure synthesis; X-ray diffraction; First-principles calculations

1. Introduction

Various scientific reasons motivate the current exploration of high-pressure (non-geologic) inorganic materials. These include:

(i) Appearance of interesting bonding situations and novel features in atomic structure [1].

(ii) Enforcing chemical bonding in systems with no or poorly pronounced compound formation at ambient pressure [2–4].

(iii) Avoiding the loss of volatile elements from the system during high-temperature treatment [5].

(iv) Testing of computational methods to predict high-pressure phases (high-pressure materials genome) [6].

Studies on intermetallic phases constitute a significant part of that research [1, 4–6].

Relatively few studies have been devoted to transition metal-Sn phases (stannides) [7], although there has been some success in preparing new phases combining late 3d metals and the lower and higher homologues of Sn, i.e. Ge and Pb [8–10]. These preparations evidently made use of a negative volume of formation of the new phases in view of the large volume of the elements.

Our own interest in the intermetallics of late transition metals and Sn is not only inspired by pure curiosity but also by the importance of such intermetallics in solder interconnects in electronic industry [11–13]. We expect that knowledge on the intermetallic phases being formed (and stable) at elevated pressures will also expand knowledge of phase stability at ambient pressure in a relevant way. This is because stable high-pressure phases may show up at ambient pressure as metastable ones or be stabilized by elemental substitution.

The equilibrium phase diagram of the Ni-Sn system at ambient pressure, relevant for the present work according to Ref. [14], is shown in Figure1(a). This diagram indicates the existence of intermetallics with the formulas Ni_3Sn (low- and high-temperature phases), Ni_3Sn_2, and Ni_3Sn_4. Note that more recent research has shown that the Ni_3Sn_2 region depicted in Fig. 1(a) actually comprises differently ordered phases within its large compositional range ($Ni_{1+\delta}Sn$, the differently ordered phases are not separately depicted in Figure 1(a); see [15]). Ni_3Sn_4 is the most Sn-rich intermetallic, which is regarded as a phase stable at ambient pressure. There are also reports about a $NiSn_4$ intermetallic developing upon metastable solidification of Sn-rich Ni-Sn melts or upon low-temperature reactive interaction between the elements [16, 17]. $NiSn_4$ appears to show differently stacked variants of its layer structure, depending on the preparation conditions [18, 19], and is most likely only metastable at ambient pressure.

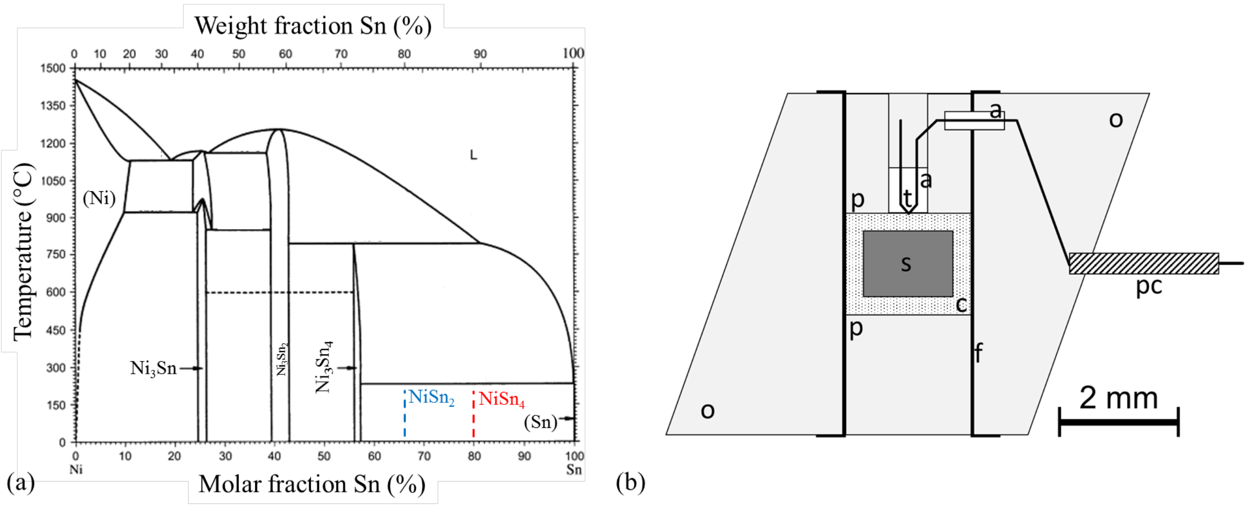

Figure 1: (a) Phase diagram of the Ni-Sn system at ambient pressure adapted from Ref. [14]. The compositions of the likely metastable $NiSn_4$ and the presently reported $NiSn_2$ high-pressure phases are indicated. (b) Schematic cross-sectional drawing of the pressure-cell employed for the high-temperature high-pressure experiments: s - specimen, c - CsCl capsule, p - m-ZrO_2 plugs, t - W/Re type C thermocouple junction, a - Al_2O_3 capillary, f - metal foil furnace (= resistive heater), o - m-ZrO_2 octahedral pressure medium, pc - Cu protective coil.

In the present paper, the preparation of a new binary $NiSn_2$ intermetallic by means of a high-pressure heat treatment is reported. The results of the experimental structure determination on that material recovered at ambient conditions are supported by first-principles calculations on energetically optimized static structures, also rationalizing the stabilization of a $NiSn_2$ phase with respect to Ni_3Sn_4 and β-Sn, the phases usually considered as stable at ambient conditions below the liquidus line.

2. Methods

2.1 First-principles calculations

The model crystal structures considered in the course of first principles calculations were the stable Ni_3Sn_4 and β-Sn structures, as well as four crystal structures with $NiSn_2$ composition: $CuAl_2$-, $CoGe_2$-, $PdSn_2$-[1] and CaF_2-type $NiSn_2$ (compare Figure 2 and Table 1). Their structures were anticipated as candidates upon inspection of the crystal structures of "late" transition metal distannides MSn_2 but also digermanides and disilicides (see also Section 4).

All first-principles calculations based on density functional theory (DFT) were performed by the Vienna *Ab initio* Simulation Package (VASP) [21]. The ion-electron interaction was described by the projector augmented wave method [22] and the exchange-correlation functional was described by the generalized gradient approximation (GGA) developed by Perdew, Burke, and Ernzerhof (PBE) [23]. Ten electrons ($3d^84s^2$) were treated as valence electrons of Ni and fourteen ($4d^{10}5s^25p^2$) of Sn. In the VASP calculations, a default plane wave cutoff energy of 269.5 eV was employed for structural relaxations in terms of the Methfessel-Paxton method [24]. Final calculations of total energies were performed by the tetrahedron method with a Blöchl correction [25] using a wave cutoff energy of 520 eV. The employed **k**-points meshes as well as the number of atoms in the supercell for each structure are listed in Sec. 2.3 (*cf.*, Table 2). The self-consistency of total energy was converged to at least 10^{-6} eV per atom. Due to the magnetic nature of pure nickel and many of its intermetallics, all calculations on Ni-containing materials were performed by spin polarization calculations assuming ferromagnetic coupling. However, only pure Ni remained spin polarized among the currently studied structures.

Lattice parameters and fractional coordinates are reported as obtained by the as-relaxed VASP calculations. Taking the atomic volume V_0^*

$(V_0^*)^{1/3}$ were performed. The resulting energy vs. volume data points for the considered structures were evaluated by a four-parameter Birch-Murnaghan (4BM) equation of state as formulated in Ref. [26]. The coefficients of that equation can directly be expressed in

---

[1] Note that in some works the orthorhombic $CoGe_2$-type structure is alternatively referred to as $PdSn_2$-type structure. In this work we use the denotations of structure types as used e.g. in ref. [20], referring the $PdSn_2$ type to the tetragonal polytype of the $CoGe_2$-type structure.

terms of the energy at the ground state E_0, the volume V_0, the bulk modulus B_0 as well as its pressure derivative B_0' at a pressure of $P = 0$ GPa (≈ ambient pressure), yielding

$$E = E_0 + \frac{9}{16} V_0 B_0 \left\{ (6 - B_0') - (16 - 3B_0')\left(\frac{V_0}{V}\right)^{\frac{2}{3}} + (14 - 3B_0')\left(\frac{V_0}{V}\right)^{\frac{4}{3}} - (4 - B_0')\left(\frac{V_0}{V}\right)^{2} \right\} \qquad (1)$$

Note that the V_0 values determined by the EOS fitting (listed in Table 2) deviate up to about 1% from the V_0^* values derived from the lattice parameters (listed in Table 1).

Table 1: Crystallographic characteristics of the model structures considered for $NiSn_2$ based on the present first-principles calculations by full relaxation of the lattice parameters together with the presently obtained experimental results from PXRD.[a]

Structure for $NiSn_2$	Space group	Fraction of 4^4 Sn layers	Lattice parameters a, b, c, Å	Axial ratio
$CuAl_2$ type	$I4/mcm$	0	6.4498, 6.4498, 5.5623	$\frac{c}{2a} = 0.431$
$CoGe_2$ type	*Aeam*[b]	1/2	6.3463, 6.3660, 11.903	$\frac{c}{4\sqrt{ab}} = 0.468$
$PdSn_2$ type	$I4_1/acd$	1/2	6.3692, 6.3692, 23.643	$\frac{c}{8a} = 0.464$
CaF_2 type	$Fm\bar{3}m$	1	6.3692, 6.3692, 6.3692	$\frac{a}{2a} = 1/2$
experimental[c]	*Aeam*[a]	1/2	6.2818, 6.2818, 11.8960	$\frac{c}{4\sqrt{ab}} = 0.471$

[a] Further details of the relaxed crystal structures may be obtained from the joint CCDC/FIZ Karlsruhe online deposition service:https://www.ccdc.cam.ac.uk/structures/? by quoting the deposition number CSD-2103460-2103463. The experimental structure model has been deposited under CSD-2103459. [b] This structure was originally described in the subgroup *Aba*2 [27] with *Aea*2 being the version according to ref. [28] using the *e* glide plane. The standard setting of the centrosymmetric supergroup taken into account in some later works [9] corresponds to a space group symbol *Cmce* (old symbol: *Cmca*) being the standard setting according to ref. [28]. That setting is also used in the CIF file CSD-2103463 whereas here the *Aeam* (old symbol: *Abam*) setting is used, being compatible with a pseudotetragonal *c* axis. [c] See Table 3 for more details.

2.2 High-pressure high-temperature heat treatments

Single-phase $Ni_{1.35}Sn$ powder obtained in a previous study [29] as well as Sn powder (Sigma Aldrich, 99.8% trace metals basis, < 45 μm) were used as starting materials. The powders were finely ground and sieved to a particle size of less than 50 μm. The powders were then mixed to yield an average composition of $Ni_{33}Sn_{67}$ and pre-pressed to a pellet of 3.0 mm diameter and 2.3 mm height. The pellet was sealed into a CsCl capsule with 0.6 mm wall thickness to prevent the specimen from oxidation during the heat treatments. The filled capsule had final dimensions of 4.2 mm diameter and 3.4 mm height.

For the heat treatment at 10 GPa and 400°C, a multi-anvil assembly of type "14/8" has been employed. This involved an octahedral pressure cell with an edge length of 14.5–14.7 mm and WC-Co anvils with 8 mm edge truncations. A cross-sectional drawing of the employed octahedral pressure cell is shown in Figure 1(b). Capsule and specimen were inserted into a central borehole in the m-ZrO_2 pressure medium, which was lined with a 65 μm Kanthal A1 foil resistive heater. The capsule was held in place by m-ZrO_2 plugs. Type C thermocouples (W5%Re/W26%Re, ConceptAlloys, Inc.) were routed concentrically through a bore in the upper plug and fixed on top of the capsule lid by a four-hole Al_2O_3 capillary (Friatec GmbH). The boreholes along the thermocouples were cemented with m-ZrO_2. All m-ZrO_2 parts were manufactured in-house. To protect the thermocouple against mechanical damage, Cu coils of 7 mm length were placed around the thermocouple and inserted approximately 1 mm deep in the pressure medium.

The samples have been pressurised in a uniaxial press with 10 MN maximum ram force, which was equipped with a Walker-type [30] multi-anvil apparatus (both Voggenreiter Sondermaschinen GmbH). The pressure scale has been calibrated in an additional calibration experiment at room temperature using a method adapted from [31] and described more closely in the Supplementary Material of Ref. [32].

Heating was started after the maximum pressure of 10 GPa (at a press force of 5.36 MN) had been reached. After heating at 400 °C for 8 h, the specimen was quenched to room temperature by switching off the power supply.

It should be noted that due to the steep thermal gradients in the small pressure cells, the placement of the thermocouple on top of the CsCl capsule can cause significant deviation of the measured temperature from the actual temperature of the specimen. Employing dedicated software [33] we estimated that the measured temperature of 400°C can indeed be in the order of 10–15% lower than the actual temperature of the specimen due to thermal gradients in the pressure cell.

2.3 Materials analysis

Powder X-ray diffraction (PXRD) data was recorded on a Bruker D8 Advance (Bruker AXS) Bragg-Brentano-type diffractometer equipped with an X-ray tube with Co anode, a quartz Johannsson-type monochromator in the incident beam to eliminate all radiation components except Co$K\alpha_1$ (wavelength λ = 1.78897 Å) and a LynxEye 1D detector in the diffracted beam. The data was recorded from a tiny piece of powdered alloy recovered from the high-pressure high-temperature treatment which was sedimented onto a (510)-cut "zero background" Si wafer in a range of $2\theta = 20\ldots140°$ with a step size of ≈ 0.01°.

The PXRD data was evaluated using the TOPAS [34, 35] software package. The background was described by a 7th order Chebyshev polynomial. Single-peak fitting on some low-angle reflections was performed with Lorentzian functions to yield fitted full-width-at-half maximum (FWHM) values. For Pawley [36] and Rietveld fits, the peak profile shapes were assessed by fitting parameters of a variant of the pseudo-Voigt function [37]. Additionally, parameters accounting for Lorentzian shaped anisotropic microstrain broadening as described in [35, 38] were refined to account for the pronouncedly *hkl*-dependent line broadening, allowing only parameters of the Gaussian part of the isotropic pseudo-Voigt function [37] to be non-zero. While the zero-error was taken fixed as 0, a specimen displacement parameter was refined.

For the scanning electron microscopy (SEM) measurements, an alloy piece was cold-embedded into epoxy resin avoiding any thermal treatment. After conventional grinding and polishing, vibrational polishing using colloidal silica (20 nm) was applied as final step. To ensure electrical conductivity, the specimen was coated by a thin carbon layer. A JEOL JSM 7800F instrument was used at a voltage of 20 kV with a beam current of 7 nA to obtain backscattered electron (BSE) images. In these, the regions (phases) with high electron densities (average atomic number) appear light, and such with low electron densities appear dark. For further phase identification electron backscattered diffraction (EBSD; Hikari Super, EDAX) and electron dispersive X-ray spectroscopy (EDS; Octane Elite, EDAX) were used. Kikuchi patterns were stored alongside to evaluate different eligible structure models (see Table 3). Apart from the $NiSn_2$ phase treated as discussed in some more detail in section 3.2, indexing was attempted for the following phases with the indicated lattice parameters for simulation of the Kikuchi patterns: β-Sn ($I4_1/amd$, a = 5.83 Å, c = 3.18 Å), Ni_3Sn_4 ($C2/m$, a = 12.20 Å, b = 4.06 Å, c = 5.22 Å, β = 105.17°) and Ni_3Sn_2 ($P6_3/mmc$, corresponding to the high-temperature HT phase, a = 4.10 Å, c = 5.18 Å).

3. Results

3.1 First-principles calculations

The relaxed lattice parameters from the first-principles calculations have been compiled in Table 1 whereas the fitted parameters of Eq. (1) have been compiled in Table 2. Drawings of the four model structures based on the relaxed structure parameters are presented in Figure 2. Figure 3(a) and 3(b) show the energy of formation values and the absolute volume V_0 values of the $NiSn_2$ model structures in comparison with the corresponding values of Ni_3Sn_4 and β-Sn, respectively.

The results of the first-principles calculations have revealed that at 0 GPa the following holds:

(i) For $NiSn_2$, the CaF_2-type structure has the lowest energy value, with the $CoGe_2$- and $PdSn_2$-type structures (which can be regarded as polytypes) having somewhat higher energies and the $CuAl_2$-type structure having the highest energy. The energy value of the CaF_2-type $NiSn_2$ is located −10.9 meV/atom below the line connecting the energy values for Ni_3Sn_4 and β-Sn, indicating its stability with respect to Ni_3Sn_4 + β-Sn, which are usually considered as the only stable phases in this compositional range.[2]

(ii) The trend in volumes of the $NiSn_2$ model structures is opposite to that for the energies: The volume for the CaF_2-type structure is the largest and that of the $CuAl_2$-type structure is the smallest. The values pertaining to all model structures except for the CaF_2 type are located below

---

[2] α-Sn with the diamond structure is not considered here, but calculations not shown here have demonstrated that CaF_2-type $NiSn_2$ is by −1.6 meV stable against Ni_3Sn_4 + α-Sn. Note that also γ-Sn [39] has not been considered in the present calculations.

the line connecting the volume values due to Ni_3Sn_4 and β-Sn, indicating that all model structures except for the CaF_2 type have a negative volume of formation with respect to Ni_3Sn_4 and β-Sn. This implies stabilization of the $CoGe_2$-, $PdSn_2$-, and $CuAl_2$-type structures at elevated pressures with respect to Ni_3Sn_4 and β-Sn.

Table 2: Results from fitting of the parameters of the equation of state in eq. (1) for the different Ni–Sn crystal structures considered in the first-principles calculations. In addition, the total number of atoms in the indicated non-primitive unit cells (uc) and the **k**-point meshes used for first-principles calculations are also listed. For the lattice parameters, see Table 1.

Structure	Space group	Atoms/uc	**k**-meshes	DFT energy E_0, eV per atom	Volume V_0, Å^3 per atom	Bulk modulus B_0, GPa	Pressure derivative of bulk modulus B_0'
Ni[c]	$Fm\bar{3}m$	4	30×30×30	–5.5699	10.943	193.8	4.91
Ni_3Sn_4	$C2/m$	7	13×10×8	–4.9114	18.389	96.6	5.22
β-Sn	$I4_1/amd$	2	18×18×31	–3.9661	28.425	47.6	4.84
Ni_3Sn_4 + β-Sn[a]	–			–4.7014[b]	20.619[b]	–	–
$CuAl_2$-type $NiSn_2$	$I4/mcm$	12	8×8×9	–4.6635	19.495	83.9	5.15
$CoGe_2$-type $NiSn_2$	$Aeam$[b]	24	6×6×3	–4.6973	20.244	82.2	4.91
$PdSn_2$-type $NiSn_2$	$I4_1/acd$	48	5×5×1	–4.6931	20.201	81.7	5.05
CaF_2-type $NiSn_2$	$Fm\bar{3}m$	12	10×10×10	–4.7123	20.861	80.6	5.93

[a] Average for mechanical mixture with $Ni_{33}Sn_{67}$ gross composition. [b] See also footnote a to Table 1. [c] Ferromagnetic spin polarization considered.

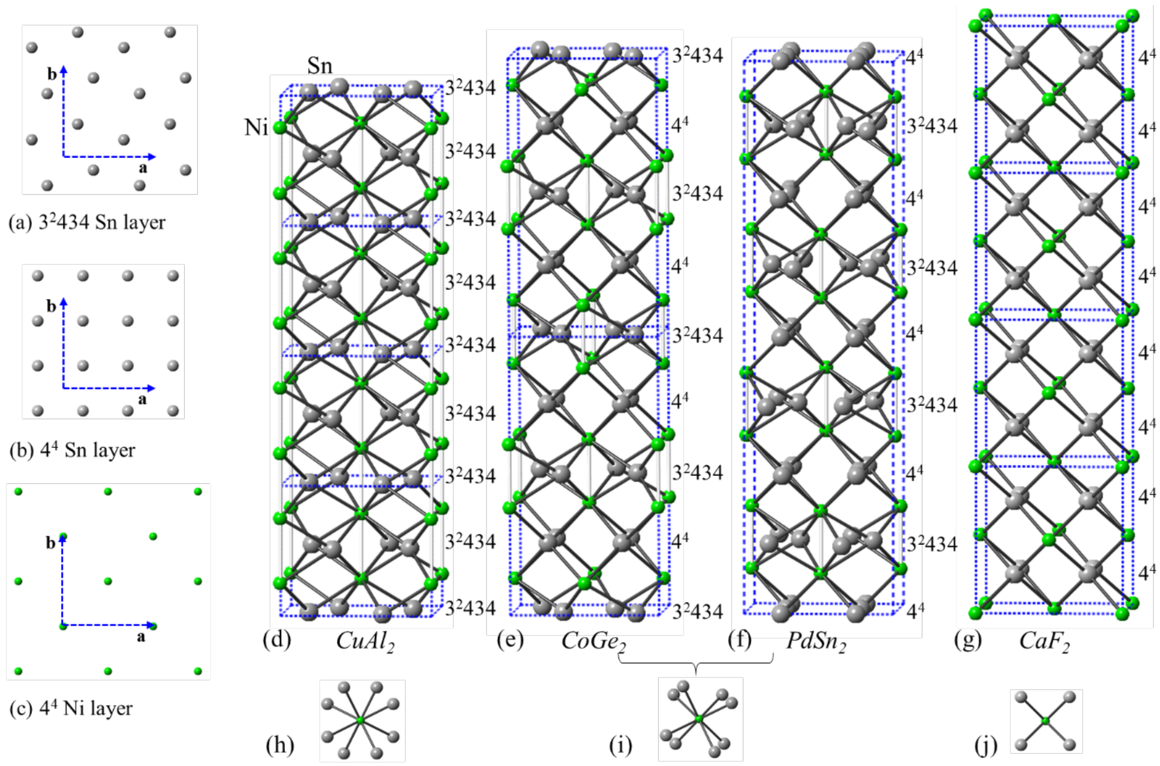

Figure 2: Illustration of the tetragonal or pseudotetragonal model structures considered for $NiSn_2$ in the present work containing (a, b) two types of Sn layers and (c) Ni layers, where the layers shown in (a, c) assume positions differently shifted perpendicular to the stacking direction. The considered structures shown in clinographic projection are (compare Table 1): (d) $CuAl_2$- ($I4/mcm$ space group symmetry), (e) $CoGe_2$- (encountered here; $Aeam$), (f) $PdSn_2$- ($I4_1/acd$; second origin choice) and (g) CaF_2-type ($Fm\overline{3}m$) structures of $NiSn_2$. All structures are represented with the c axis pertaining to the chosen space group setting (Table 1) aligned in vertical orientation and depicting always a part of a crystal comprising 8 Sn layers. The coordination of Ni by 8 Sn atoms is depicted in (h)–(j). Note that the unit cells have different kinds of origins depending on the space group setting used for the respective structure.

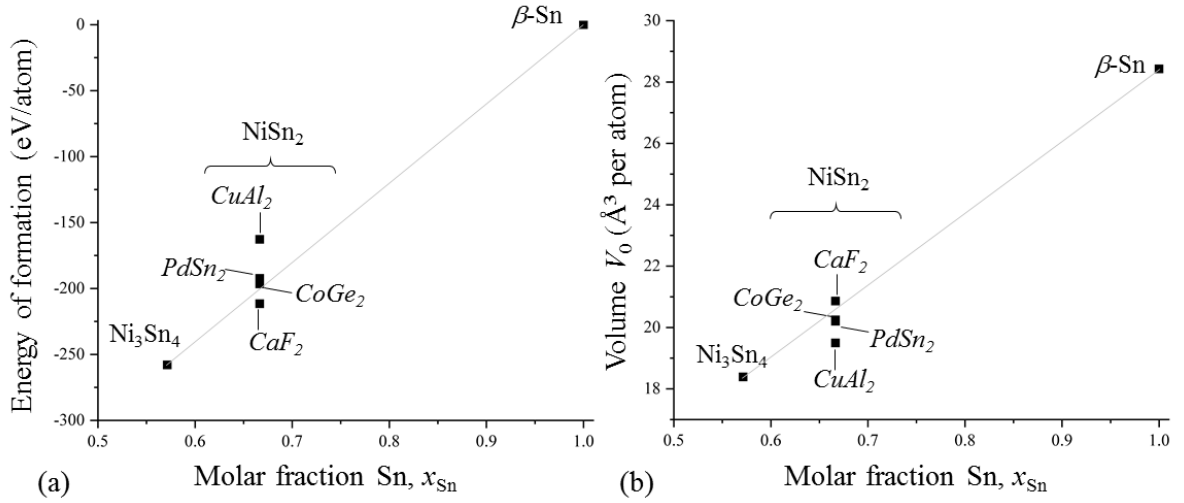

Figure 3: Results DFT-based first-principles calculations of Ni_3Sn_4 and *β*-Sn as well as of $NiSn_2$ with structures according to the prototypes (in italics) listed in Table 1 and 2: (a) Energy of formation values calculated from the E_0 values of the indicated structures and the E_0 values of Ni and *β*-Sn and (b) absolute volumes V_0 at a pressure of 0 GPa. The differences between the $NiSn_2$ points and the grey lines connecting the values for Ni_3Sn_4 and *β*-Sn allow discerning the energy and volume of formation of the respective $NiSn_2$ structures from a mixture of Ni_3Sn_4 + *β*-Sn.

3.2 Experimental results

A series of EDX analyses conducted at different locations on the cross-section of the high-pressure heat-treated alloy revealed that the majority of the sample volume had a uniform composition of $NiSn_{2.08\pm0.06}$. Remaining Sn- and Ni-rich regions, which are well visible as lighter and darker regions upon backscattered contrast imaging (see Figure 4(a)), were identified as *β*-Sn and Ni_3Sn_2 by means of EBSD (see Figure 4(b, c)). Kikuchi patterns from thin rims surrounding the Ni_3Sn_2 particles could not be indexed by any reasonable phases. This is most likely due to the tiny crystallites leading to Kikuchi pattern superposition and thus failure of indexing. We suppose the presence of Ni_3Sn_4 in these regions. Simultaneous presence of these Sn- and Ni-rich regions imply incomplete inter-diffusion during the high-pressure high-temperature treatment.

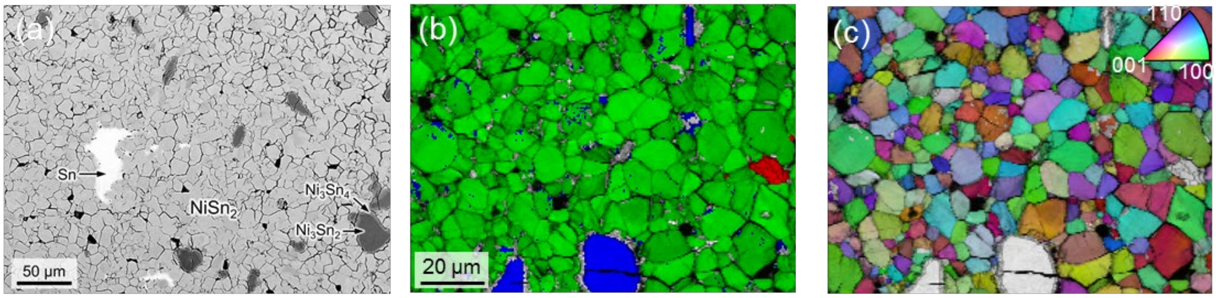

Figure 4: Scanning electron microscopy analysis of the microstructure of the $Ni_{33}Sn_{67}$ alloy after high-pressure high-temperature heat treatment at 10 GPa and 400°C. (a) Image taken with backscattered electron contrast, (b) EBSD phase map showing $NiSn_2$ in green, Ni_3Sn_2 in blue, and β-Sn. Grey regions (band contrast) include Ni_3Sn_4 being likely too finely crystalline to allow indexing. (c) EBSD inverse pole figure map for $NiSn_2$ with respect to the sample surface with the color key in the upper left corner. Non-$NiSn_2$ regions are shown in grey (band contrast). $NiSn_2$ could be indexed equally well with the $CoGe_2$- and $PdSn_2$-type structures. Indexing was eventually done using the $PdSn_2$-type structure to avoid pseudosymmetric orientation solutions; see text.

The chemical composition of the intermetallic, which complies with the stoichiometric $NiSn_2$, eased interpretation of the PXRD data. By comparison with the tetragonal or pseudotetragonal $CuAl_2$-, $CoGe_2$-, and $PdSn_2$-type structures, it turned out that the strongest Bragg reflections at 2θ = 33.1°, 47.5°, and 49.0° in the powder X-ray diffraction data (see Figure 5) were indeed compatible with such (pseudo)tetragonal structures.

Single-peak fits performed with Lorentz functions yielded peak widths which vary discontinuously with the diffraction angle (see Figure 5(a), light blue numbers), implying complicated microstructural origin of the broadening. The small amount of powder incompletely covering the irradiated area of the sample holder causes a 2θ-dependent overshoot of the irradiated area, which is difficult to reproduce accurately with an instrumental standard[3]. In any case, we refrained from assessing the instrumental line broadening, which would be a prerequisite for quantitative interpretation of anisotropic line broadening. Instead, for the following Pawley and Rietveld refinements we used a combination of isotropic Gaussian and anisotropic Lorentzian line broadening as indicated in Section 2.3 to describe the peak shapes.

---

[3] This irregular distribution of a thin powder layer also will have its effect on the refined atomic displacement parameter.

Full evaluation of the PXRD data then revealed that all clearly visible Bragg reflections can be explained by the presence of a $CoGe_2$-type $NiSn_2$ structure, which is not the case for the other considered structures for $NiSn_2$. Rietveld refinements reveal, however, that there is only limited agreement achievable between the observed and calculated reflection intensities. Attempts to introduce variable site occupation (as e.g. used in ref. [27] for this structure type) or split positions (as e.g. used in ref. [20]) did not resolve the issues. Further, it was not possible to attribute the discrepancies between observed and calculated intensities by diffraction contributions from β-Sn, Ni_3Sn_2 or Ni_3Sn_4 detected in small fractions in the course of the SEM analysis (see Figure 4).

Structural parameters were determined as follows:

Pawley fits were performed while restricting $a = b$ for the corresponding lattice parameters, considering absence of discernible splitting of e.g. the 200/020 reflections (see Figure 5(a)). Note, moreover, that the presence of anisotropic microstrain broadening obstructs accurate determination of independent lattice parameters from severely overlapping reflections [40]. Furthermore, but actually not strictly necessary (due to the robust treatment of correlated parameters), the intensities of the *hkl* and *khl* reflection pairs predicted due to space group symmetry, occurring at the same peak position, were constrained to be identical. Reflections having very small calculated intensity according to the $CoGe_2$-type structure model for $NiSn_2$ (e.g., taking the parameters from the first-principles calculations) being located in the vicinity of other strong reflections, were fixed to zero intensity. By using this procedure, it is avoided that observed intensity is described with “wrong” reflections, which may lead to inappropriate values of the refined lattice parameters as a result of the Pawley refinement with otherwise freely refined reflection intensities. This measure was required due to the presence of relatively broad reflections in combination with a large number of available reflection positions compatible with unit cell and space group. A comparison between the observed and calculated profiles is shown in Figure 5(b).

The lattice parameters determined by means of Pawley fits are compiled in Table 3. The lattice parameters and parameters describing the line broadening were held fixed and used in the subsequent Rietveld refinements. The texture was treated conservatively by refining one parameter within a March-Dollase model [41].

True Rietveld refinement was then performed with a conservative texture model giving the results listed in Table 3 and the fit as displayed in Figure 5(c). The limited agreement between observed and calculated integrated reflection intensities is probably due to an incomplete consideration of structural disorder including layer faulting leading to complicated modifications of the intensity profile. Nevertheless, it appears that the produced $NiSn_2$ is, on the average, of the $CoGe_2$-type structure. Validity of that structure is additionally supported by the close agreement of the lattice parameters from experiments and the first-principles calculations (order of 1 % or less). Deeper insight into the atomic structure (including planar faulting) could be provided by means of local methods like transmission electron microscopy with selected area diffraction and high-resolution imaging. Note that investigation of the ground powder did not reveal pronouncedly anisotropic shapes of the powder particles or signs of plastic deformation due to the grinding process.

It was possible to index the Kikuchi patterns obtained from the $NiSn_2$ regions taken in the course of the SEM investigations (Figure 4) using the $CoGe_2$-type structure model determined by PXRD (see Table 3). During indexing two orientations differing mutually by a rotation of 90° around the [001] direction result in basically identical reliability parameters. This implies tetragonal pseudosymmetry of the orthorhombic $CoGe_2$-type structure. Closer analysis has revealed that e.g. the 21*l*/12*l* bands of the orthorhombic structure breaking the tetragonal pseudosymmetry are not visible. Their masking can be caused by the strong higher-order 42*l*/24*l* bands (not breaking the pseudosymmetry). Smearing of the 21*l*/12*l* bands can also be caused by planar faulting. Moreover, faulting in the stacking sequence can in particular lead to 90° twinning on (001) planes on a fine scale, making the diffraction pattern macroscopically tetragonal. In fact, it turns out that indexing is also successful with the tetragonal $PdSn_2$-type structure for $NiSn_2$ (using a *c* lattice parameter twice as long as for the $CoGe_2$-type structure), as the diffraction patterns of the $PdSn_2$- and $CoGe_2$-type structures mainly differ by the 21*l*/12*l* bands invisible in the present Kikuchi patterns. As a unique orientation solution results upon indexing with the tetragonal $PdSn_2$-type structure, this structure was used to evaluate the Kikuchi patterns in terms of crystallite orientation revealing a well-recrystallized microstructure with globular grains as it concerns the $NiSn_2$ phase, see Figure 4(b,c).

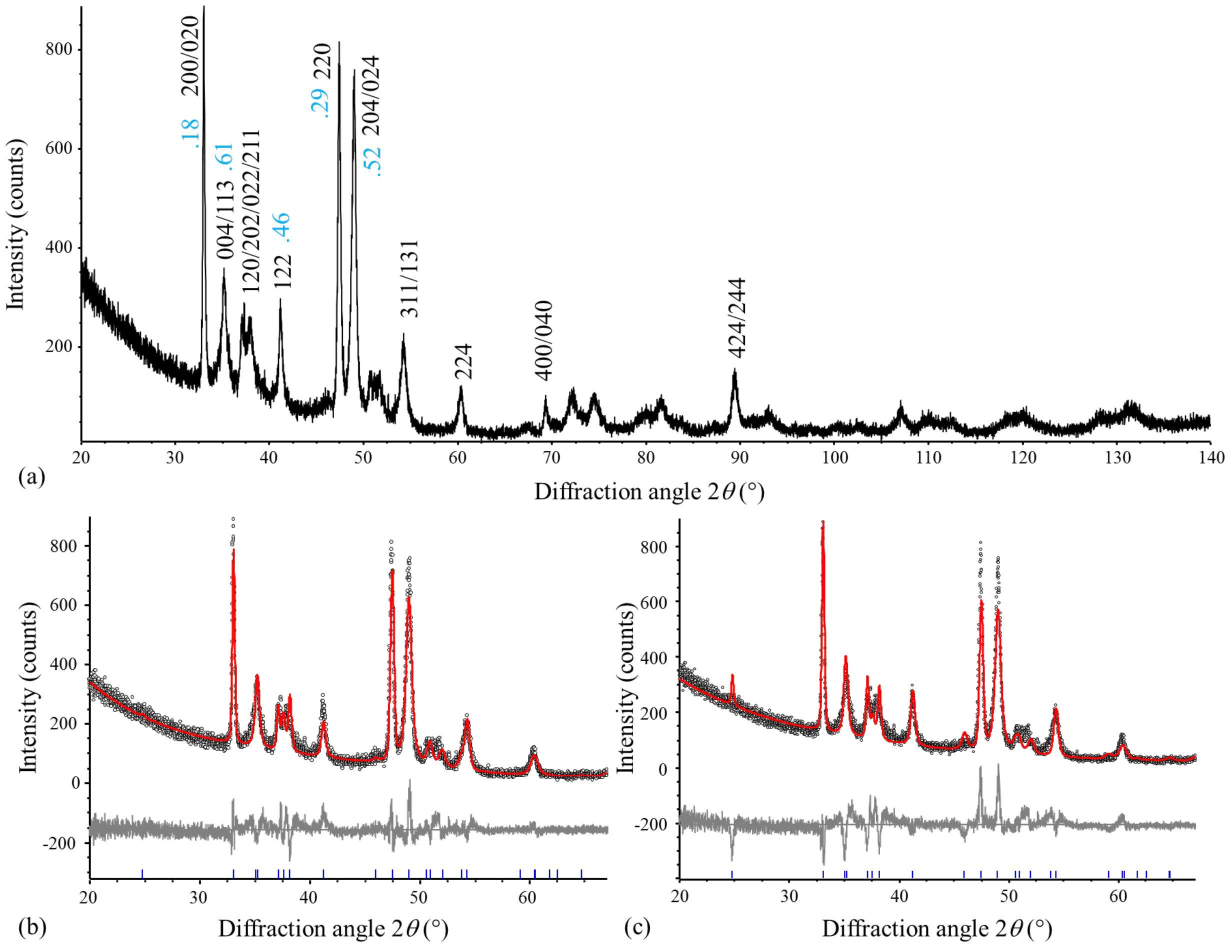

Figure 5: Powder X-ray diffraction data (Co$K\alpha_1$ radiation) of the Ni$_{33}$Sn$_{67}$ alloy recovered from the high-pressure heat temperature treatment at 400°C and 10 GPa. The XRD data indicate that the crystal structure of the resulting NiSn$_2$ phase is of CoGe$_2$ type. (a) Overview with the scan as a black line and with some reflections labelled with *hkl*-indices pertaining to the pseudo-tetragonal unit cell employing the *Aeam* setting, with the 122 reflection being, in particular, characteristic for the assessed structure type. Light blue numbers give the full-width-at-half-maximum values determined by single-peak fitting hinting at anisotropic line broadening. Results of (b) Pawley and (c) Rietveld refinement shown for a low-angle region of the scan with observed profile as black data points, red lines for the calculated profiles and grey lines at the bottom to indicate the difference curve, respectively.

Table 3: Most important results of Pawley and subsequent Rietveld refinements of $CoGe_2$-type $NiSn_2$ based on powder X-ray diffraction data shown in Figure 5 (using the *Aeam* setting of the space group symmetry).

Pawley refinement	
Lattice parameters[a]	$a = b = 6.2818$ Å $c = 11.8960$ Å
Residual parameters	$R_{wp} = 0.137$, $R_p = 0.104$
Rietveld refinement	
Lattice parameters	as from Pawley refinement
Atomic site, Wyckoff symbol, fractional coordinates $x\ y\ z$[b]	Ni, 8*d*, 0 0 0.1131(8) Sn1, 8*f*, 0.3086(5), 0.1719(5), 0 Sn2, 1/4 0.2518(4) 1/4
March-Dollase fitting parameter for texture [41]	Consideration of 001 texture with the parameter amounting 1.091(4)
Residual parameters	$R_{wp} = 0.181$, $R_p = 0.137$

[a] Due to the high number of data points, an unnaturally small value of the standard deviation of the lattice parameters is obtained. Here the lattice parameters are given with a precision of 0.0001 Å. [b] A single common atomic displacement parameter was refined for all atoms leading to $B = 0.55(5)$ Å^2. This value is definitely affected by the small amount of powder (beam overspill) and a most likely incomplete structure model implied by the incomplete description of the observed intensity profile by the used model, see text and Figure 5.

4. Discussion

Is has been shown that a high-pressure high-temperature heat treatment at 10 GPa and 400°C of a Ni_3Sn_2+Sn powder mixture with a nominal composition of $Ni_{33}Sn_{67}$ results in the formation of a new intermetallic phase $NiSn_2$. The intermetallic recovered from the multi-anvil experiment has a faulted pseudotetragonal $CoGe_2$-type structure. This crystal structure type has been described previously as a mixed structure between CaF_2 and $CuAl_2$ type [20, 27, 42], as illustrated in Figure 2. In the (cubic) CaF_2-type structure (see Figure 2(g)) only layers with squares of tin atoms (vertex symbol 4^4 [43], Figure 2(a)) exist, with Ni atoms arranged in layers as depicted in Figure 2(c) which are enclosed in a cubic environment by Sn (see Figure 2(j)). In contrast, the $CuAl_2$-type structure (see Figure 2(d)) consists of combined square/triangular Sn layers (vertex symbol 3^2434, Figure 2(b)) with Ni atoms enclosed in a square antiprismatic environment (see Figure 2(h)). While the Ni layers are identical in the $CuAl_2$- and CaF_2-type structures in Figure 2(c), their stacking differs. The Ni layers are directly stacked above each other in the case of the $CuAl_2$-type structure, leading to short Ni–Ni distances along the stacking direction. A distance of $c/2 = 2.78$ Å is obtained taking into account the results of the first-principles calculations, which is sufficiently short to be relevant for chemical bonding [44, 45]. Such bonds are depicted as grey solid lines in Figure 2(d). In contrast, in the CaF_2-type structure the Ni layers are mutually shifted by **a**/2 or by **b**/2 avoiding such short Ni–Ni pairs.

In the $CoGe_2$-type structure there is an alternate sequence of 4^4 and 3^2434 Sn layers (see Figure 2(e)), leading to modified square antiprismatic environments of Ni by Sn and isolated short Ni–Ni pairs parallel to the *c* axis (see Figure 2(i)). The $PdSn_2$-type structure (see Figure 2(f)) is also of mixed character, but differs from $CoGe_2$ in terms of the lateral positions of the 3^2434 Sn layers. For more detailed considerations on the stacking sequences of the discussed structures, see [20, 42].

It is instructive to calculate the ratio of the average spacing of the 3^2434 Sn layers and the geometric average of the two basis vector lengths (*a* and *b* in the chosen space group settings) perpendicular to the stacking direction, in short, the *axial ratio*. As shown in Table 1, this value increases with an increasing fraction of 4^4 Sn layers. As it might be expected from the good agreement between lattice parameters from experiments and first-principles calculations (see section 3.2), the predicted and experimentally determined axial ratios for $CoGe_2$-type $NiSn_2$ agree well. In contrast, the predicted axial ratios for $CuAl_2$- and CaF_2-type $NiSn_2$ do not agree with the experimentally determined value.

The $CoGe_2$-type crystal structure has not only been observed for $CoGe_2$ [27] but also for isoelectronic $NiGe_2$ [9], being a lower homologue of $NiSn_2$. $NiGe_2$ has first been prepared by treatment of a Ni-Ge alloy at elevated pressure. In later work $NiGe_2$ could also be obtained by means of non-equilibrium procedures conducted at ambient pressure [46, 47]. Ternary variants of the structure type have been produced at 0 GPa in $Ni(Ge_{1.56}Al_{0.44})$ [48] and $NiGe_{1.5}Ga_{0.5}$ [49].

Most notably, $Co_{1-x}Ni_xSn_2$ ($0.23 < x < 0.53$) also can be produced in the $CoGe_2$-type structure whereas the structurally closely related tetragonal $PdSn_2$-type polytype is obtained under modified experimental conditions [20]. In contrast, binary $CoSn_2$ has a $CuAl_2$-type crystal structure [45]. Hence, a structure change occurs relative to $CoSn_2$ towards a ternary $Co_{1-x}Ni_xSn_2$ solid solution at some value $x > 0$, while this solid solution did not include the binary $NiSn_2$ at 0 GPa [20]. The extension to the binary $NiSn_2$ end-point has now been achieved under high-pressure conditions (see however, the discussion on polymorphism below). Some $Co_{1-x}Ni_xSn_2$ solution starting at $CuAl_2$-type $CoSn_2$ but not extending to $NiSn_2$ has also been reported in refs. [50, 51]. Note, that in this latter experimental/theoretical work a structural change as reported for

$CuAl_2$-type $CoSn_2$ was not considered/reported [20], and no evidence excluding such a structure change was provided.

As discussed in detail in ref. [20, 52], the experimentally determined crystal structures of transition metal distannides evolve systematically with increasing electron number supplied by the transition metal in terms of $CuMg_2 \rightarrow NiMg_2 \rightarrow CuAl_2 \rightarrow CoGe_2$.[4] When additionally considering the digermanides and disilicides of the late 3d transition metals (Fe…Ni; see Table 4, i.e. not taking into account the earlier transition metals as candidates for $CuMg_2$- or $NiMg_2$-type distannides), it becomes evident that for a given transition metal element (in particular Co), the sequence of structure types appears to be continued towards the CaF_2 type upon going from Sn and Ge to the smaller Si atoms. The observed structure types compiled in Table 4 imply that the preferred structure type is not only a pure consequence of electron count but likely also a function of atomic size.

Table 4: Overview of known late 3d transition metal disilicides, digermanides and distannides. Cu does not appear in such compounds. Likewise, diplumbides of the listed transition metals are unknown.

	Si	Ge	Sn[b]
Mn	–	$CuAl_2$ [54]	$CuAl_2$ [55]
Fe	CaF_2-related [56]	$CuAl_2$ [57]	$CuAl_2$ [58]
Co	CaF_2 [59]	$CoGe_2$ [27]	$CuAl_2$ [58]
Ni	CaF_2 [27]	$CoGe_2$[a] [9]	($CoGe_2$)[c]

[a] First prepared under high-pressure conditions, but also obtained by different means at ambient pressure. [b] As considered in more detail previously [52], the earlier distannides (Cr, ….) feature the $CuMg_2$ and, in a small window of electron-to-atom ratios also the $NiMg_2$ structures. [c] Present work, possibly $CuAl_2$ type at the given pressure-temperature regime.

As mentioned in Section 3.1, the first-principles calculations reveal that the energy values E_0 of $NiSn_2$ in the $CuAl_2$-, $CoGe_2$-, $PdSn_2$-, and CaF_2-type structures differ only slightly (see Table 2 and Figure 3(a)), with the CaF_2-type $NiSn_2$ structure attaining the lowest energy at 0 GPa. As deduced from the volumes (see Table 2 and Figure 3(b)), it may be expected that the energetic hierarchy changes significantly upon increasing pressure. This energetic hierarchy with increasing pressure P can be assessed by comparison of the enthalpy $H(P)$ values amounting to

---

[4] In line with the above-mentioned $Co_{1-x}Ni_xSn_2$ series [20], $NiSn_2$ can also be regarded as the yet unknown end member of the $Cr_{1-x}Ni_xSn_2$ explored in ref. [53], yielding in that work, apart from $CuMg_2$-type $CrSn_2$, also a $NiMg_2$-type $Cr_{0.83}Ni_{0.17}Sn_2$ and an $CuAl_2$-type $Cr_{0.75}Ni_{0.25}Sn_2$.

$$H(P) = E(V(P)) + PV(P) \qquad (2)$$

For that purpose, based on the volume derivative of Eq. (1), amounting to $-P = \mathrm{d}E/\mathrm{d}V$, $V(P)$ values up to 12 GPa have been obtained and used for the calculation of $H(P)$. In Figure 6, the values relative to the mechanical mixture Ni_3Sn_4 + β-Sn with average composition of $Ni_{33}Sn_{67}$/$NiSn_2$ have been plotted. The full lines give the values according to Eq. (2), whereas the dashed line shown exemplarily for CaF_2 shows the evolution resulting from the approximation $H(P) = E_0 + PV_0$ valid for incompressible solids (see e.g. [6]). The calculated values of $H(P)$ predict that the CaF_2-type $NiSn_2$ is stable up to about 4.0 GPa, where it should transform into $CoGe_2$-type $NiSn_2$ and further into $CuAl_2$-type $NiSn_2$ at about 7.7 GPa.

Evidently, the encounter of a $CoGe_2$-type $NiSn_2$ as the product of the high-pressure high-temperature heat treatment at 10 GPa and 400°C needs to be reconciled with the predicted stability of $CuAl_2$-type $NiSn_2$ at $P \geq 7.7$ GPa from the first-principles calculations. These calculations basically pertain to the static structures at 0 K (i.e., not considering the zero-point vibrational energy; in short: "0 K prediction").

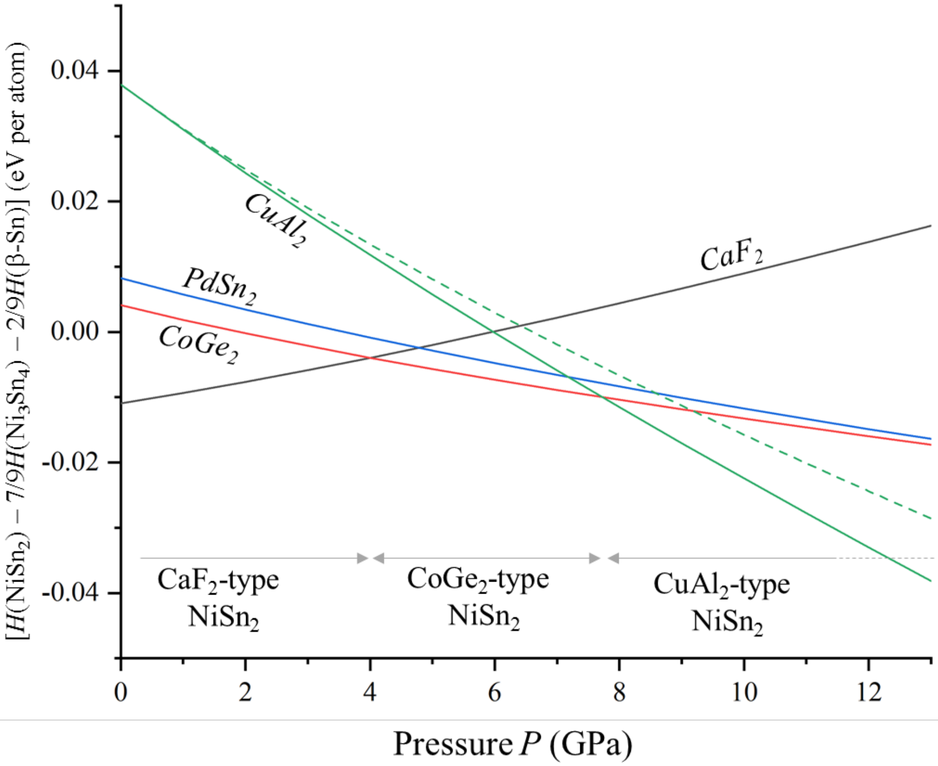

Figure 6: Evaluation of the pressure-dependent enthalpy of formation of the four different $NiSn_2$ model structures (type in italics) with respect to the value pertaining to a mechanical mixture Ni_3Sn_4 + β-Sn. The most stable $NiSn_2$ structure in a certain range of pressure is indicated at the bottom. The solid lines are calculated according to Eq. (2). The dashed line exemplarily shows the results for the approximation $H(P) = E_0 + PV_0$ (see text).

If one assumes that the $CoGe_2$-type structure $NiSn_2$ recovered *after* the high-pressure high-temperature treatment was already present *during* this treatment, this would contradict the "0 K prediction" (predicting a $CuAl_2$-type $NiSn_2$ at 10 GPa). To explain this discrepancy, one may consider an overestimation of the pressure present during the treatment, which, however, seems unlikely. The applied assessment of the pressure does not include the *thermal pressure* caused by the thermal expansion partially suppressed under high-pressure conditions. In that sense the 10 GPa given here is a lower limit for the actual pressure acting at 400°C.

Alternatively, one may assume that the low-volume $CuAl_2$-type structure of $NiSn_2$ was indeed present at 10 GPa and 400°C and transformed to the $CoGe_2$-type structure upon cooling or upon release of the pressure by a thermally activated shear/shuffle mechanism. This scenario is supported by the existence of other binary systems in which a $CuAl_2$-type structure seems to be stabilized as the high-temperature phase against other structures. The first example to be mentioned is rhodium distannide, $RhSn_2$. $CuAl_2$-type $RhSn_2$ appears to be a high-temperature polymorph above about 500°C [27]. This high-temperature polymorph of $RhSn_2$ consisting exclusively of 3^2434 Sn layers appears to transform more or less readily upon cooling towards polymorphs containing CaF_2-type layers [27, 42]. A partially disordered six-layer polytype with a 1/3 fraction of 4^4 Sn layers has been reported in [42], and a $CoGe_2$-type polytype (1/2 4^4 Sn layers) has also been described [27].[5] Theoretical results from a second example, copper dialuminide $CuAl_2$ itself, provide further insight. In that case it has been revealed by means of first-principles calculations on static structures comparable to those conducted here for $NiSn_2$ that the CaF_2-type $CuAl_2$ has a lower energy than the experimentally well-established $CuAl_2$-type $CuAl_2$ [60] which is usually regarded as the equilibrium phase down to low temperatures. This

---

[5] Notably, the lattice parameters reported for these polymorphs reveal the same increase of the axial ratio with increasing CaF_2-layer fraction as implied here by the results on the first-principles calculations of the various $NiSn_2$ structures (see Table 2).

has been explained with a high-temperature vibrational-entropic stabilization of the $CuAl_2$-type $CuAl_2$ due to characteristic soft phonon modes not available in CaF_2-type $CuAl_2$. If this argument is valid also for intermetallics like $NiSn_2$ or $RhSn_2$, this would imply high-temperature stabilization with respect to polymorphs containing CaF_2-like 4^4 Sn layers like the $CoGe_2$-type structure. Hence, if the prediction of a stable $CuAl_2$-type $NiSn_2$ at 10 GPa and 0 K based on the first-principles calculations is valid, it is expected from the aforementioned findings that the stability of $CuAl_2$-type $NiSn_2$ against the other three model structures is even enhanced by the elevated temperature of 400°C.

A relatively rapid transformation towards the $CoGe_2$-type $NiSn_2$ from a $CuAl_2$ polymorph e.g. upon cooling, may also explain the faulted character of its crystal structure implied by the PXRD data and, to some extent, by the EBSD analysis. (Synchro-)shear/shuffle mechanisms changing stacking sequences can, in fact, lead to characteristic faulting in the resulting structure, which need not comply with equilibrium, as e.g. worked out previously in case of transformations between different Laves phase polytypes [61, 62].

All these factors that may have an influence on the relative stability of the series of structure types $CuAl_2$, $CoGe_2$/$PdSn_2$, and CaF_2, have been summarized in Figure 7. The stabilization of the $CoGe_2$-type structure against the $CuAl_2$-type structure with its increased number of electrons has already been pointed out in ref. [52] and the extension to the CaF_2-type structure is proposed based on the increasing fraction of 4^4 Sn layers.

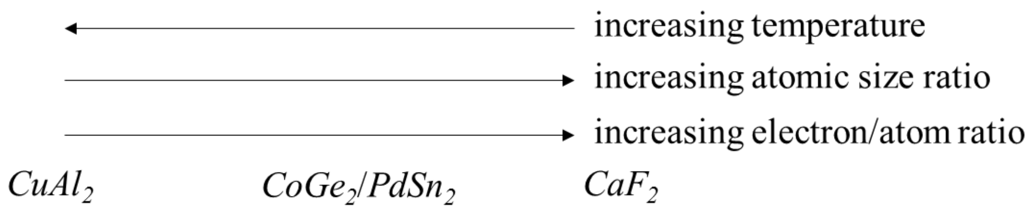

Figure 7: The factors that influence the structure types (in italics) of late transition metal disilicides, digermanides and distannides considered for $NiSn_2$ derived from Table 4 and from the trends encountered for $RhSn_2$ [27, 42] and $CuAl_2$ [60]; see also text.

5. Conclusions

High-pressure high-temperature treatment of a $Ni_{33}Sn_{67}$ pre-alloy at 10 GPa and 400°C leads to the formation of a yet unknown $NiSn_2$ intermetallic with $CoGe_2$-type crystal structure. First-principles calculations performed on a series of $NiSn_2$ model structures support the experimental observations, predicting (for 0 K) the stability of a CaF_2-type $NiSn_2$ observed against Ni_3Sn_4 + β-Sn, followed by $CoGe_2$-type $NiSn_2$ above 4.0 GPa and $CuAl_2$-type $NiSn_2$ above 7.7 GPa. The latter fact supports that the $CuAl_2$-type structure might be stable at 10 GPa and 400°C, such that the observed $CoGe_2$-type $NiSn_2$ is the product of a polymorphic transition upon cooling or decompression. From literature analysis of $CuAl_2$-type intermetallics, it is expected that the $CuAl_2$ type is additionally stabilized by vibrational entropy with respect to the $CoGe_2$ type. The scenario of a potential polymorphic transition is further supported by the defective character of the structure suggested by the pronounced line broadening observed in the powder diffraction data.

In any case, the formation of a $NiSn_2$-type phase at elevated pressures reveals that the existence of distannides of the earlier 3d transition metals up to Co can be extended for Ni, and that previously reported series of ternary distannides like $Cr_{1-x}Ni_xSn$ and $Co_{1-x}Ni_xSn$ also include $NiSn_2$.

Acknowledgements: SLS and ZKL acknowledge the financial support by the U.S. National Science Foundation (NSF) with Grant No. CMMI-1825538. First-principles calculations were performed on the resources of the National Energy Research Scientific Computing Center (NERSC) supported by the U.S. Department of Energy, Office of Science User Facility operated under Contract No. DE-AC02-05CH11231.

References

1. Demchyna R., Leoni S., Rosner H., Schwarz U. *Z. Kristallogr.* 2006, *221*, 420–423. https://doi.org/10.1524/zkri.2006.221.5-7.420

2. Wang X., Liu X. *Inorg. Chem. Front.* 2020, *7*, 2890–2908. https://doi.org/10.1039/D0QI00477D

3. Tse J. S. *Natl. Sci. Rev.* 2020, *7*, 149−169. https://doi.org/10.1093/nsr/nwz144

4. Walsh J. P. S., Freedman D. E. *Acc. Chem. Res.* 2018, *51*, 1315−1323. https://doi.org/10.1021/acs.accounts.8b00143

5. Range K.-J. *Chem. Unserer Zeit* 1976, *10*, 180−188. https://doi.org/10.1002/ciuz.19760100604

6. Amsler M., Hegde V. I., Jacobsen S. D., Wolverton C. *Phys. Rev. X* 2018, *8*, 41021 (18 pages). https://doi.org/10.1103/PhysRevX.8.041021

7. Pöttgen, R., Johrendt D. *Intermetallics: Synthesis, Structure, Function*, De Gruyter Textbook. De Gruyter: Berlin 2014.

8. Tamerius A. D., Clarke S. M., Gu M., Walsh J. P. S., Esters M., Meng Y., Hendon C. H., Rondinelli J. M., Jacobsen S. D., Freedman D. E. *Angew. Chem. Int. Ed.* 2018, *57*, 12809−12813. https://doi.org/10.1002/anie.201807934

9. Takizawa H., Uheda K., Endo T. *J. Alloys Compd.* 2000, *305*, 306–310. https://doi.org/10.1016/S0925-8388(00)00733-7

10. Takizawa H., Sato T., Endo T., Shimada M. *J. Solid State Chem.* 1990, *88*, 384–390. https://doi.org/10.1016/0022-4596(90)90232-M

11. Tu K. N., Zeng K. *Mater. Sci. Eng. R* 2001, *34*, 1–58. https://doi.org/10.1016/S0927-796X(01)00029-8

12. Mu D. K., McDonald S. D., Read J., Huang H., Nogita K. *Curr. Op. Sol. Stat. Mater. Sci.* 2016, *20*, 55–76. https://doi.org/10.1016/j.cossms.2015.08.001

13. Laurila T., Vuorinen V., Kivilahti J. K., *Mater. Sci. Eng. R* 2005, *49*, 1–60. https://doi.org/10.1016/j.mser.2005.03.001

14. Schmetterer C., Flandorfer H., Richter K. W., Saeed U., Kauffman M., Roussel P., Ipser H. *Intermetallics* 2007, *15*, 869–884. https://doi.org/10.1016/j.intermet.2006.10.045

15. Leineweber A. *Int. J. Mater. Res.* 2011, *102*, 861–873. https://doi.org/10.3139/146.110540

16. Boettinger W. J., Vaudin M. D., Williams M. E., Bendersky L. A., Wagner W. R. *J. Electr. Mater.* 2003, *32*, 511–515. https://doi.org/10.1007/s11664-003-0135-x

17. Hou N., Belyakov S. A., Pay L., Sugiyama A., Yasuda H., Gourlay C. M. *Acta Mater.* 2018, *149*, 119–131. https://doi.org/10.1016/j.actamat.2018.02.034

18. Schimpf C., Kalanke P., Shang S.L., Liu Z. K., Leineweber A. *Mater. Design* 2016, *109*, 324–333. https://doi.org/10.1016/j.matdes.2016.07.002

19. Leineweber A., Wolf C., Kalanke P., Schimpf C., Becker H., Shang S. L., Liu Z. K. *J. Alloys Compd.* 2019, *774*, 265–273. https://doi.org/10.1016/j.jallcom.2018.09.341

20. Häussermann U., Landa-Cánovas A. R., Lidin S. *Inorg. Chem.* 1997, *36*, 4307–4315. https://doi.org/10.1021/ic9703134

21. Kresse G., Furthmüller J. *Phys. Rev. B* 1996, *54*, 11169–11186. https://doi.org/10.1103/PhysRevB.54.11169

22. Kresse G., Joubert D. *Phys. Rev. B* 1999, *59*, 1758–1775. https://doi.org/10.1103/PhysRevB.59.1758

23. Perdew J. P., Burke K., Ernzerhof M. *Phys. Rev. Lett.* 1996, *77*, 3865–3868. https://doi.org/10.1103/PhysRevLett.77.3865

24. Methfessel M., Paxton A. T. *Phys. Rev. B* 1989, *40*, 3616–3621. https://doi.org/10.1103/PhysRevB.40.3616

25. Blöchl P. E., Jepsen O., Andersen O. K. *Phys. Rev. B* 1994, *49*, 16223–16233. https://doi.org/10.1103/PhysRevB.49.16223

26. Shang S.-L., Wang Y., Kim D., Liu Z.-K. *Comp. Mater. Sci.* 2010, *47*, 1040–1048. https://doi.org/10.1016/j.commatsci.2009.12.006

27. Schubert K., Pfisterer H. *Z. Metallkd.* 1950, *41*, 433–441. https://doi.org/10.1515/ijmr-1950-411111

28. Hahn T., Ed. *International tables for crystallography*, 5th ed. Springer: Dordrecht 2005.

29. Leineweber A. *J. Sol. State Chem.* 2004, *177*, 1197–1212. https://doi.org/10.1016/j.jssc.2003.10.028

30. Walker D., Carpenter M. A., Hitch C. M. *Am. Mineral.* 1990, *75*, 1020–1028.

31. Schwarz M. R. *J. Phys.: Conf. Ser.* 2010, *215*, 12193 (10 pages). https://doi.org/10.1088/1742-6596/215/1/012193

32. Wetzel M. H., Rabending T. T., Friák M., Všianská M., Šob M., Leineweber A. *Materials* 2021, *14*, 3963 (27 pages) https://doi.org/10.3390/ma14143963

33. Hernlund J., Leinenweber K., Locke D., Tyburczy J. A. *Am. Mineral.* 2006, *91*, 295. https://doi.org/10.2138/am.2006.1938

34. TOPAS (version 5.0). *General profile and structure analysis software for powder diffraction data*, Bruker AXS: Karlsruhe (Germany), 2014.

35. Dinnebier R. E., Leineweber A., Evans J. S. O. *Rietveld Refinement*. De Gruyter: Berlin, Boston 2018.

36. Pawley G. S. *J. Appl. Crystallogr.* 1981, *14*, 357–361. https://doi.org/10.1107/S0021889881009618

37. Thompson P., Cox D. E., Hastings J. B. *J. Appl. Crystallogr.* 1987, *20*, 79–83. https://doi.org/10.1107/S0021889887087090

38. Leineweber, A. *Z. Kristallogr.* 2011, *226*, 905–923. https://doi.org/10.1524/zkri.2011.1413

39. Barnett J. D., Bean V. E., Hall H. T. *J. Appl. Phys.* 1966, *37*, 875–877. https://doi.org/10.1063/1.1708275

40. Leineweber A. *Powder Diffr.* 2017, *32*, S35-S39. https://doi.org/10.1017/S0885715617000665

41. Dollase W. A. *J. Appl. Crystallogr.*1986, *19*, 267–272. https://doi.org/10.1107/S0021889886089458

42. Hellner E. *Z. Kristallogr.* 1956, *107*, 99–123. https://doi.org/10.1524/zkri.1956.107.1-2.99

43. Blatov V. A., O’Keeffe M., Proserpio D. M. *CrystEngComm* 2010, *12*, 44–48. https://doi.org/10.1039/B910671E

44. Yannello V. J., Fredrickson D. C. *Inorg. Chem.* 2015, *54*, 11385−11398. https://doi.org/10.1021/acs.inorgchem.5b02016

45. Armbrüster M., Schnelle W., Cardoso-Gil R., Grin Y. *Chem. Eur. J.* 2010, *16*, 10357–10365. https://doi.org/10.1002/chem.201001473

46. Al-Joubori A. A., Suryanarayana C. *Mater. Des.* 2015, *87*, 520–526. https://doi.org/10.1016/j.matdes.2015.08.051

47. Lim P. S. Y., Chi D. Z., Lim P. C., Wang X. C., Chan T. K., Osipowicz T., Yeo Y.-C. *Appl. Phys. Lett.* 2010, *97*, 182104 (3 pages). https://doi.org/10.1063/1.3514242

48. Reichmann T. L., Duarte L. I., Effenberger H. S., Leinenbach C., Richter K. W. *Intermetallics* 2012, *28*, 84–91. https://doi.org/10.1016/j.intermet.2012.04.002

49. Panday P. K., Schubert K. *J. Less-Comm. Met.* 1969, *18*, 175–202. https://doi.org/10.1016/0022-5088(69)90157-X

50. Chen C.-C., Chan Y.-T., Chen Y.-T. *J. Mater. Res.* 2010, *25*, 1321–1328. https://doi.org/10.1557/JMR.2010.0168

51. Bi X., Hu X., Li Q., Li Y. *Results Phys.* 2019, *14*, 102439 (10 pages). https://doi.org/10.1016/j.rinp.2019.102439

52. Häussermann U., Simak S.I., Abrikosov I. A., Johansson B., Lidin S. *J. Am. Chem. Soc.* 1998, *120*, 10136–10146. https://doi.org/10.1021/ja981347t

53. Larsson A.-K., Lidin S. *J. Alloys Compd.* 1995, *221*, 136–142. https://doi.org/10.1016/0925-8388(94)01412-4

54. Gutiérrez-Naranjo D., Holguín-Momaca J. T., Solís-Canto Ó. O., Gupta P., Poddar P., Magaña F. E., Olive-Méndez S. F. *Thin Sol. Films* 2018, *657*, 38–41. https://doi.org/10.1016/j.tsf.2018.05.007

55. Dong Y., DiSalvo F. J. *Acta Crystallogr.* 2005, *E61*, i282–i284. https://doi.org/10.1107/S1600536805038092

56. Dusausoy Y., Protas J., Wandji R., Roques B. *Acta Crystallogr.* 1971, *B27*, 1209–1218. https://doi.org/10.1107/S0567740871003765

57. Havinga E.E., Damsma H., Hokkeling P. *J. Less-Comm. Met.* 1972, *27*, 169–186. https://doi.org/10.1016/0022-5088(72)90028-8

58. Armbrüster M., Schmidt M., Cardoso-Gil R., Borrmann H., Grin Y. *Z. Kristallogr. - New Cryst. Struct.* 2007, *222*, 83–84. https://doi.org/10.1524/ncrs.2007.0033

59. Krendelsberger N., Weitzer F., Schuster J.C., Stein F. *Intermetallics* 2013, *38*, 92–101. https://doi.org/10.1016/j.intermet.2013.02.021

60. Wolverton C., Ozolinns V. *Phys. Rev. Lett.* 2001, *86*, 5518–5521. https://doi.org/10.1103/PhysRevLett.86.5518

61. Aufrecht J., Baumann W., Leineweber A., Duppel V., Mittemeijer E. J. *Phil. Mag.* 2010, *90*, 3149–3175. https://doi.org/10.1080/14786435.2010.482068

62. Aufrecht J., Leineweber A., Duppel V., Mittemeijer E. J. *J. Mater. Res.* 2010, *25*, 1983–1991. https://doi.org/10.1557/JMR.2010.0265